Tribology International 188 (2023) 108833

Contents lists available at ScienceDirect

Tribology International

journal homepage: www.elsevier.com/locate/triboint

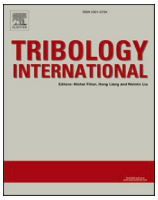

Artificial neural network for tilting pad journal bearing characterization

Edoardo Gheller [a,*], Steven Chatterton [a], Daniele Panara [b], Gabriele Turini [b], Paolo Pennacchi [a]

[a] Department of Mechanical Engineering, Politecnico di Milano, Via G. la Masa 1, 20156 Milan, Italy
[b] Baker Hughes, Via Felice Matteucci 2, 50127 Florence, Italy

ARTICLE INFO

Keywords:
Artificial Neural Network
Deep Learning
Lubrication
Tilting Pad Journal Bearings

ABSTRACT

Tilting pad journal bearings (TPJBs) are modeled with Reynold-based models or computational fluid dynamics (CFD) approach. In both cases, the estimation of the dynamic coefficients of the oil-film forces and the static characteristic, can be computationally expensive and time consuming. Artificial Intelligence (AI) is assuming a key role in engineering but is rarely applied in fluid film bearing analysis. A properly trained Deep Learning (DL) model can perform very fast predictions of TPJB behavior with accuracy comparable to more time-consuming models. In this case, the main drawback is the time required to build the training dataset. In this work, an Artificial Neural Network (ANN) is trained to predict the dynamic stiffness and damping coefficients along with the main static quantities of TPJBs, such as minimum oil-film thickness and inlet flowrate. At first, a design of experiment is performed to build an appropriate training dataset. Secondly, a Reynolds-based thermo-hydrodynamic (THD) model is used to populate the training dataset and an appropriate test dataset. Then, a feed-forward ANN is trained with Levenberg–Marquardt backpropagation and its architecture is optimized to increase accuracy. Finally, the accuracy of the ANN is tested using the test dataset and experimental data. The time and computational effort required by the ANN regression are much less than those required by the THD model. Therefore, the trained ANN is an effective and efficient tool for the characterization of TPJBs.

1. Introduction

Tilting Pad Journal Bearings (TPJBs) are used extensively in many industrial applications, especially in power generation and oil & gas industry. The evaluation of their static and dynamic characteristics is fundamental. At the design stage, static characteristics such as oil-film thickness, pressure, and temperature allow the functioning of these components to be monitored. The characterization of dynamic properties, such as stiffness and damping coefficients, is essential for rotor dynamic analysis of turbomachinery equipped with oil-film bearings.

Modeling of TPJBs is generally performed with two approaches. The first is based on the Reynolds equation. The latter is based on computational fluid dynamics (CFD). In [1,2] the authors developed a three-dimensional model of TPJBs based on the Reynolds equation for the evaluation of the pressure distribution in the oil film. Moreover, the three-dimensional energy equation is solved by considering the heat exchange of the oil with both the pad and the shaft. The effect of elastic and thermal deformation of the shaft and pads is also considered together with the flexibility of the pivot. In [3,4] the authors developed a model equivalent to the one presented in [1,2] but based on a three-dimensional CFD model of the same TPJB considering both the thermal and elastic deformations of the pads and shaft. The flexibility of the pivot is also considered in the simulation. Both approaches ensure great accuracy in predicting both static and dynamic characteristics of TPJBs. However, the computational time required to complete a simulation is not negligible. Both the Reynolds-based model and the CFD model can be impractical in a day-to-day application or if the characterization of several bearing configurations is required. Therefore, both industrial and academic research would benefit from developing a fast-predicting tool with the same level of accuracy as a detailed model.

In the current era, if there is sufficient data characterizing a TPJB, it could be cost-effective to train a machine learning (ML) model that can predict the static and dynamic behavior of the bearing. Many applications of machine learning and artificial intelligence in tribology are present in the literature, [5,6]. From the thorough literature review presented in [5], it seems that ML is mainly applied in the fields related to composite materials, manufacturing process and surface engineering. As reported in [5], the most common application of AI for bearings is related to rolling element bearing failure and defect detection. Also in [6], the minority of papers focus on fluid film lubrication. A classifier for

* Corresponding author.
E-mail address: edoardo.gheller@polimi.it (E. Gheller).

https://doi.org/10.1016/j.triboint.2023.108833
Received 6 June 2023; Received in revised form 19 July 2023; Accepted 24 July 2023
Available online 26 July 2023

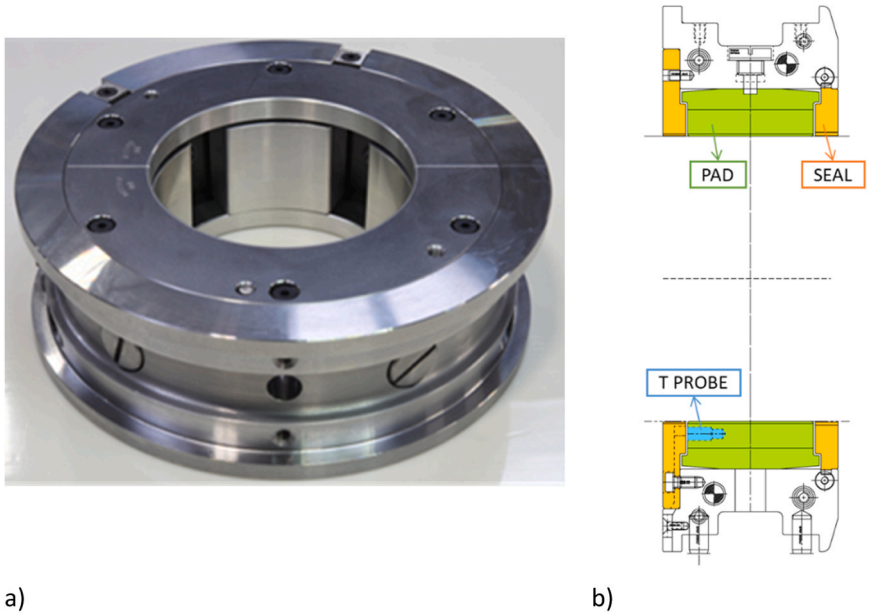

Fig. 1. Tilting pad journal bearing considered for the analysis (a), section of TPJB considered with temperature probe (b).

the fluid film bearing lubrication regime is built using the torque data in [7]. In [8], the authors test different ANN architectures for fault diagnosis for rotating machines equipped with oil film bearings, where the models are trained using experimentally measured time series.

Of course, different machine learning models can be adopted as surrogate models. In [9] the authors test several machine learning regression models to predict the load capacity of a tilting pad thrust bearing. The machine learning models are trained with data from a 2D Reynolds equation model. In [10], the same authors extended the work presented in [9] considering incomplete oil profiles. However, in case of large input and output vector size, the application of a neural network can be beneficial.

In [11], the authors proposed a machine learning model to evaluate the mixing coefficient in the region between the pads of TPJBs. The authors trained an ANN from a dataset based on CFD simulations of the region between the pads to estimate the mixing coefficient. This parameter is used to estimate the oil temperature at the leading edge of the pad for models based on the Reynolds equation. This approach is followed in [12,13] where the ANN model is linked to a Reynolds equation model to evaluate the TPJB characteristics and study the Morton effect. In [14], the complete temperature distribution at the leading edge of the pad is estimated with a deep convolutional autoencoder trained with data coming from CFD simulations of the region between the pads. In [15], they include the CNN autoencoder in a rotor-bearing model to study the Morton effect. The model is then validated with experimental results. In general, the ANN models proposed in [11,14] are both coupled with the Reynolds-based model to predict the static and dynamic performances of the bearing. In this way, a hybrid model between the one proposed in [1,2] and the one proposed in [3,4] is developed.

Table 1
Parameters describing the bearing family.

PARAMETERS	VALUES
Diameter	80–200 mm
Clearance Range	Reduced, Large
L/D ratio	0.44, 0.7
Load configuration	LOP, LBP
Oil type	ISO VG 32, ISO VG 46
Tolerance	Minimum, Maximum

In [16], the authors built a simple ANN to predict the maximum pressure in a sliding bearing considering as input the bearing aspect ratio and the normalized slider slope. After fine-tuning the network architecture, the authors achieve optimal prediction accuracy.

Another application of an ANN as a surrogate bearing model is presented in [17]. In this case, the ANN is used in conjunction with Monte Carlo simulation to assess the effect of stochasticity in a two-lobe journal bearing. The eccentricity ratio, preload value, bearing clearance, supply pressure, oil viscosity and surface roughness are considered to be the source of the uncertainty.

In [18,19] the authors use ANNs as the surrogate model of the bearing for the control of the active hydrodynamic bearing. In [18] the methodology is applied to conical bearings. In [19] the methodology is applied to a sleeve bearing with four feed chambers.

In the papers mentioned above, the trained ANN is used to predict only some bearing parameters, such as load capacity and friction torque. Moreover, the ANN applications found in the literature are highly specific. In this work, an ANN is proposed for the prediction of the static and dynamic characteristics of a family of flooded TPJBs. Therefore, the ANN will represent a surrogate model capable of predicting bearing characteristics considering all possible geometrical configurations and operating conditions of the studied TPJB family. Due to the large number of inputs and outputs required for this task, ANN is considered as the optimal choice other machine learning tools. Initially, a design of experiments phase is performed. The optimal size of the training dataset is determined by a trade-off between the accuracy of the ANN and the size of the training dataset. The training dataset is computed with a THD Reynolds-based model. Then, the ANN architecture is tuned to improve accuracy. Finally, the ANN predictions are compared with a test dataset computed with the same model as the training dataset and with some available experimental results from mechanical running tests. The proposed architecture is effective and accurate in predicting the static and dynamic characteristics of TPJBs. Therefore, the obtained ANN is able to describe the behavior of the entire TPJB family. Moreover, with the trained ANN it is possible to obtain the static characteristics of the bearing and the dynamic force coefficients with a much lower computational time than that required both by the Reynolds model presented in the paper and by the CFD model. The trained ANN is a useful tool when the bearing characteristics need be evaluated multiple times. For example, during the rotordynamic analyses of a rotating machine.

Table 2
TPJB operating conditions parameters.

Parameters	Values
Inlet pressure	0.3–2 barG
Inlet temperatures	40–55 °C
Specific load	0.3–1.5 MPa
Shaft speed	3000 rpm-75 m/s

2. Material and Methods

2.1. Bearing family

The activity is focused on the characterization of a flooded family of five-pads rocker-back TPJBs, see Fig. 1a. The pads are fully immersed in the oil and a sealing element is fitted to limit the flow rate of oil leaving the bearing. A temperature probe is installed in each pad to monitor the bearing operation, see Fig. 1b.

The bearing family is characterized by different diameters and other geometrical characteristics and parameter, as listed in Table 1.

The clearance range parameter identifies the nominal dimensions referred to both the pads and the bearing bore which, together with the assembly and machining tolerances of the pads and the shaft, uniquely determine the micro geometry of the tilting pad bearing. The clearance range is chosen based on the dynamic behavior of the rotor and bearing by the design engineer. To limit bearing design variability, only two clearance ranges have been provided to account for project-to-project variability in rotor geometry. The average assembly clearance range is approximately 1.4–1.5 [0/00] for the large clearance case, while for the reduced clearance case it is approximately 1.1–1.2 [0/00]. An average preload of approximately 0.55 is considered for both clearance ranges which determines the definition of the nominal pad bore. The clearance range parameter strongly affects both the static and dynamic performances of the TPJB, therefore it must be considered in the analysis. The manufacturing tolerances of the diameters of the sealing element, the shaft and the pad have been also considered, together with the assembly tolerance. The ends of the manufacturing tolerance range provide the minimum and maximum temperature and flowrate. For this reason, the minimum and maximum tolerance configurations are considered as input of the ANN.

The six parameters listed in Table 1 are considered as input parameters for the ANN. However, the characterization of the bearing is also determined by the operating conditions. The ranges of the four parameters characterizing the operating conditions are listed in Table 2. The inlet pressure and inlet temperature are related to the inlet conditions of the oil supplied to the bearing. The specific load and shaft speed are related to the machine in which the bearing is installed. For the shaft speed a minimum value of 3000 rpm and maximum value of 75 m/s on the tangential speed have been considered.

2.2. Bearing model

The bearing model is a thermo-hydrodynamic model based on the Reynolds equation [20,21]. The 2-dimensional pressure distribution in each oil-film is calculated by means of the well-known Reynolds equation:

$$\frac{\partial}{\partial x}\left(\frac{\rho h^3}{12\mu}\frac{\partial p}{\partial x}\right)+\frac{\partial}{\partial z}\left(\frac{\rho h^3}{12\mu}\frac{\partial p}{\partial z}\right)=\frac{\partial}{\partial x}\left(\rho h\frac{u_1+u_2}{2}\right)-\rho u_2\frac{\partial h}{\partial x}+\rho(v_2-v_1) \tag{1}$$

where x is the tangential direction, z is the axial direction, h is the oil-film thickness, p is the pressure in the oil-film, μ is the oil dynamic viscosity, and ρ is the oil mass density. The velocity vector components of the shaft and the pads are described by u_1, v_1 and u_2, v_2, respectively, where u represents the velocity component along the tangential direction (x coordinate) and v the velocity component along the radial direction (y coordinate). At steady state: $u_1 = \Omega R$ and $v_1 = u_2 = v_2 = 0$, where Ω is the rotational speed and R is the shaft radius.

The oil viscosity and density are modeled as a function of the temperature T:

$$\begin{aligned}\mu &= a_\mu \cdot e^{-b_\mu T}+c_\mu \cdot e^{-d_\mu T}\\ \rho &= a_\rho \cdot T+b_\rho\end{aligned} \tag{2}$$

where the parameters a_i, b_i, c_μ and d_μ are obtained by fitting the data of two oils with different viscosities considered in the analysis, namely ISO VG 32 and ISO VG 46 oils. The cavitation problem is solved as a Linear Complementarity Problem, [22,23]. Please refer to [21] for a more detailed description. Due to the considerable number of simulations planned for the construction of the training dataset required by the network, a simple 2-dimensional temperature model has also been considered for the oil film. A more accurate temperature distribution can be obtained by using a 3D thermal model for the oil film with adiabatic conditions at shaft and pads interfaces, in combination with a generalized Reynolds equation that accounts for the change in viscosity in the thickness direction of the oil. A further step in the direction of accuracy can be achieved by including heat exchanges in the shaft and pads. Finally, considering the scope of the paper, a trade-off between the accuracy of the model and the total time required for the construction of the training database, has been assumed. Therefore, without loss of generality, the widely used 2D Reynolds equation and 2D thermal model for the oil film have been used. The pressure and temperature models are iteratively solved until convergence to evaluate the viscosity distribution for use in Eq. (1).

For the 2D thermal model, the adiabatic condition is assumed at the shaft and pad interfaces. Assuming laminar flow, the heat generated in the oil-film due to viscous stresses is considered in the energy equation as follows:

$$\rho\, c_{OIL}\left(u\frac{\partial T}{\partial x}+w\frac{\partial T}{\partial z}\right)=k_{OIL}\left(\frac{\partial^2 T}{\partial x^2}+\frac{\partial^2 T}{\partial z^2}\right)+\mu\left[\left(\frac{\partial u}{\partial y}\right)^2+\left(\frac{\partial w}{\partial y}\right)^2\right] \tag{3}$$

where z and w are the axial coordinates and velocity respectively. k_{OIL} and c_{OIL} are the thermal conductivity and the heat capacity of the oil, respectively, that are modelled as:

$$\begin{aligned}k_{OIL} &= a_k \cdot T+b_k\\ c_{OIL} &= a_c \cdot T+b_c\end{aligned} \tag{4}$$

where the parameters a_k, b_k, a_c and b_c are obtained by fitting the data of two oils. The Reynolds and the energy equations have been integrated using a finite difference method. The supplied oil pressure is assumed at all edges of the oil film as the boundary condition for integrating the Reynolds equation. For integrating the energy equation, an adiabatic condition is assumed for both sides and the trailing edge of the oil film, whereas an inlet temperature is assumed at the leading edge of the oil film. The inlet temperature T_i^k of the k-th pad, is obtained from the mixing that takes place in the groove of two consecutive pads between the hot oil of the previous (k-1)-th pad and the cold supplied oil, considering the mass balance and energy equations in each groove, as follows [21]:

$$T_i^k=\frac{(\dot m\cdot c_{OIL})_o^{k-1}T_o^{k-1}+\left[(\dot m\cdot c_{OIL})_s^{k-1}-\beta\cdot(\dot m\cdot c_{OIL})_g^{k-1}\right]T_s}{(1-\beta)(\dot m\cdot c_{OIL})_g^{k-1}+(\dot m\cdot c_{OIL})_i^{k-1}} \tag{5}$$

where $\dot m$ is the mass flow rate, the suffix "o" refers to outlet quantities at trailing edge, "i" at leading edge, "s" to the known supplied quantities and β is the mixing coefficient defined as follows:

$$\beta=1-\frac{\dot m_o^{k-1}}{\dot m_s^k} \tag{6}$$

It is also assumed that the total mass flow rate supplied in the bearing $\dot m_s$ is equally distributed between the pads, as $\dot m_s^k = \dot m_s/N$.

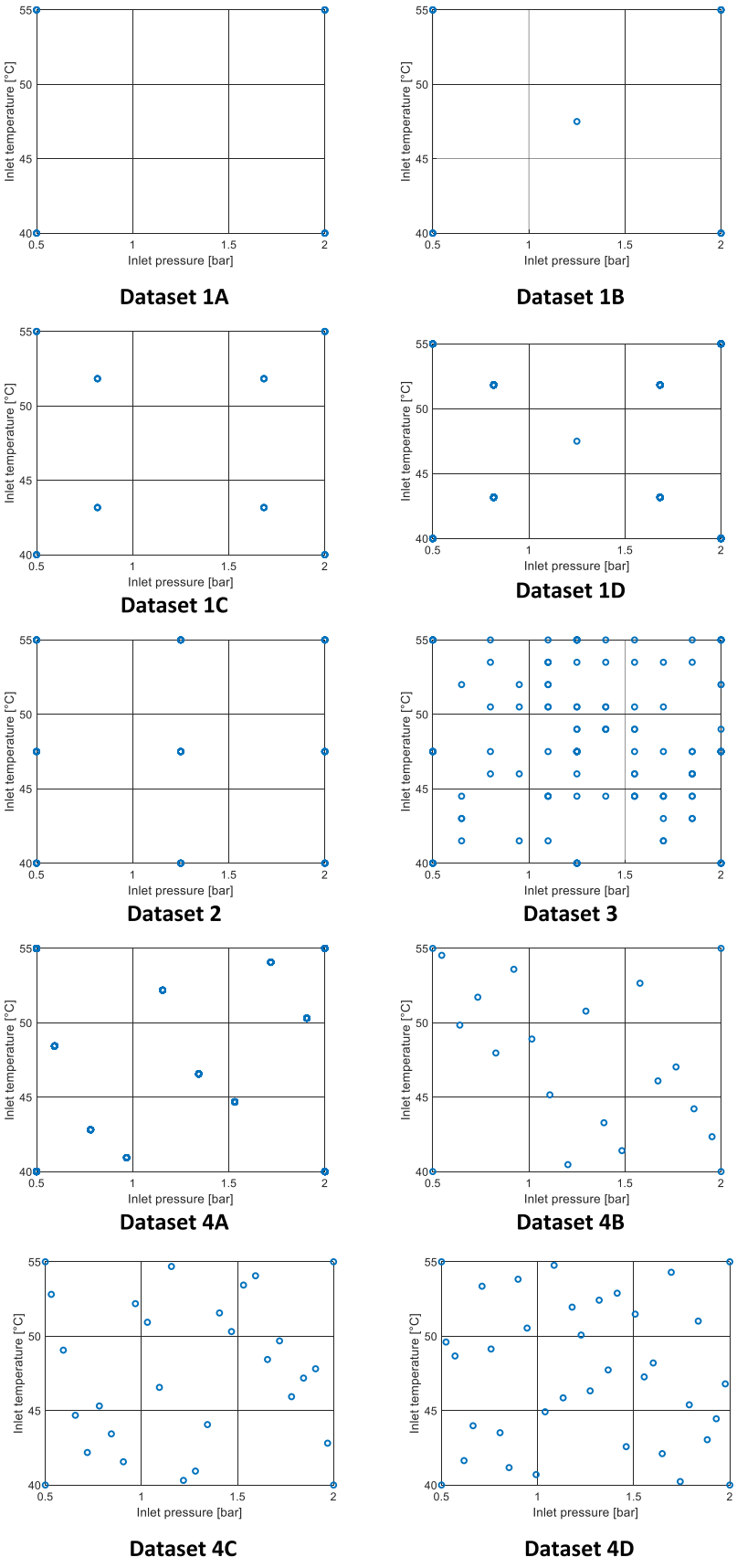

Fig. 2. Graphical representation of the different approaches followed for creating the training dataset.

Table 3
Description of the databases shown in Fig. 2.

Dataset	Description	Total number of points
1 A	Full factorial level 2	$16 * 2^4 = 256$
1B	SET 1 A + middle point	$256 + 16 = 272$
1 C	2 × 2 full factorial level 2	$16 + 2^5 = 512$
1D	SET 1 C + middle point	$528 + 16 = 528$
2	Full factorial level 3	$16 * 3^4 = 1296$
3	SET 2 + around 1000 points randomly selected	2250
4 A	Full factorial level 2 + LHS 8	$16 * (2^4 + 8) = 384$
4B	Full factorial level 2 + LHS 16	$16 * (2^4 + 16) = 512$
4 C	Full factorial level 2 + LHS 24	$16 * (2^4 + 24) = 640$
4D	Full factorial level 2 + LHS 32	$16 * (2^4 + 32) = 768$

The total supplied flow rate Q_s is determined by the supplied oil pressure p_s and the geometry of the two seals. Considering the seals centered with respect to the bearing, the oil-film thickness in each seal can be approximated as $h \approx c[1 + k\cos(\phi)]$, where c is the radial clearance of the seal and k is the eccentricity ratio of the shaft. Assuming a laminar flow regime in the seal and a constant pressure, equal to the supplied pressure p_s, in the portion of oil that fills the bearing from the supplied holes to the seals, the total flow rate Q_s of the two identical seals can be evaluated as:

$$Q_s \approx 2\rho \frac{\pi c^3 \left[\left(3k^4/8 + 3k^2 + 1\right)c + \left(3k^2 + 2\right)R\right]}{12\mu L}(p_s - p_{atm}) \tag{7}$$

where L is the seal length,R is the radius of the shaft and p_{atm} is the ambient pressure. The mass density and viscosity of the oil that exits the bearing from the seals depend on the outlet temperature T_o from the bearing that can be obtained from the dissipated power W_{loss} as follows:

$$W_{loss} = Q_s \int_{T_s}^{T_o} \rho(T) c_p(T) dT \tag{8}$$

Equations from (5) to (8) are solved iteratively until convergence. The estimation of the probe temperature installed in each pad is obtained by a 3-dimensional thermal model of the pad, that gives the temperature in the entire pad, as follows:

$$\nabla(k_{PAD} \nabla T) = 0 \tag{9}$$

where k_{PAD} is the thermal conductivity coefficients of the pad. Steel is considered for the base part of the pad and white metal for the pad lining. The temperature distribution in each oil film, obtained from the 2D thermal model, is assumed as boundary condition at the oil interface. Convective boundary conditions are assumed for all the others surfaces in contact with the lubricating oil at supply temperature T_s. The 3D thermal model for the pad only is solved by a finite element approach.

2.3. Design of experiments for database training

The training dataset is obtained from a finite number of simulations that can be generated by the combination of the parameters listed in Table 1 and Table 2. The parameters in Table 1 can assume discrete values producing a finite number of combinations. On the contrary, the parameters in Table 2 can produce an infinite number of combinations since each parameter can vary continuously over the given range. The size of the training dataset is therefore strongly influenced by the number of operating conditions considered in the training dataset. The more points considered, the more detailed the characterization of the space defined by the extremities of the operating conditions, and the greater the computational time required to create the training dataset. A trade-off is therefore considered to maximize the accuracy of the ANN while minimizing the computation time.

The investigation of the dataset creation strategy was performed considering the case of the 80 mm bearing. As already mentioned in Section 2.1, for the 80 mm bearing, the ratio L/D = 0.44 is fixed and is not considered as a parameter. Therefore, the discrete parameters are clearance, load configuration, oil type, and tolerance type. Each of these parameters can assume two configurations, therefore the number of combinations is $N_1 = 2^4 = 16$.

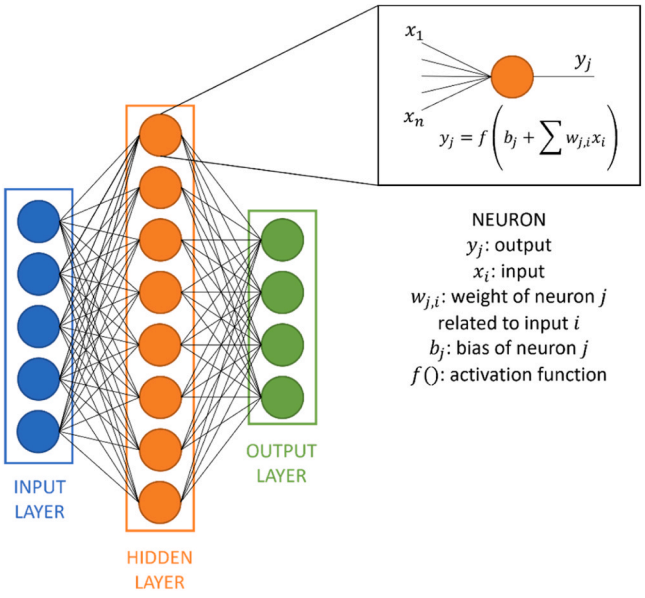

Fig. 3. Representation of the feed forward neural network.

In total, 10 different strategies have been evaluated for the continuous parameters of Table 2. In Fig. 2, the blue dots represent the value of the quantities considered for the creation of the database. Only inlet temperature and pressure are shown, but the same considerations apply for specific load and shaft speed. The total number of combinations listed in Table 3 is given by the product of the combinations N_1 of the parameters in Table 1 and the combinations N_2 considered for the parameters in Table 2.

From dataset 1 A to dataset 3, the full-factorial approach is considered and adding some extra points. The other datasets from 4 A to 4D are based on both the full factorial and Latin Hypercube Sampling (LHS) approaches. The LHS approach guarantees a generation of points distributed randomly and uniformly in space. Dataset 1 A is obtained from a level 2 full factorial in which only the extremes of the available range are considered. Dataset 1 C is obtained by from a level 2 full-factorial considering the range boundaries and Gaussian points located at 21.13% and 78.87% of the range. The addition of the midpoint in dataset 1B and dataset 1D is to reduce the polarization of the database towards the edges of the operating field. Dataset 2 is obtained from a level 3 full-factorial, while dataset 3 is obtained from dataset 2 by adding about 1000 random points where each parameter can assume 10 fixed points equidistant in the available range. Full factorial points are included to dataset 4 s to populate the dataset at the margin of the operating field. As mentioned above, due to the large number of

Table 4
Inputs and outputs of ANN.

Input	Output
1. Diameter	1. Max pad temperature
2. L/D Ratio	2. Probe temperature
3. Clearance	3. Oil out temperature
4. Tolerance	4. Power loss
5. Load Direction	5. Minimum oil film thickness
6. Oil Type	6. Inlet flowrate
7. Inlet Temperature	7. Dynamic stiff. coeff. $\begin{bmatrix} K_{xx} & K_{xy} \\ K_{yx} & K_{yy} \end{bmatrix}$
8. Inlet Pressure	
9. Specific Load	8. Dynamic damping coeff. $\begin{bmatrix} C_{xx} & C_{xy} \\ C_{yx} & C_{yy} \end{bmatrix}$
10. Shaft Speed	

simulations to be run to build each dataset, the analysis of the training dataset preparation was carried out only for the 80 mm bearing.

2.4. Artificial Neural Network

In this work, we have considered several ANN architectures. Matlab Deep Learning Toolbox was used to build, train, and test the ANNs, [24]. For this task, feed forward neural networks with fully connected layers and different number of neurons have been analyzed. An example of the network architecture is shown in Fig. 3. The inputs and outputs of the ANN are listed in Table 4. The linearized dynamic stiffness and damping coefficients have been evaluated by means of the synchronous reduced approach.

The training is performed with the Levenberg-Marquardt algorithm, [25]. A split dataset is assigned in the training phase. 80% of the training dataset is kept for training, 15% is used for validation and 5% for testing. The mean squared error is assigned as the loss function to be minimized. During the training procedure the neuron weights and biases are updated to minimize loss function. Network performance is evaluated on the validation split and training is interrupted if validation performance does not decrease with epochs.

The clearance, tolerance, load configuration and oil type parameters are not numerical. Since they can take on only two values, they are transformed into a binary number before training. All diameters of the bearing family are considered (80, 90, 100, 110, 130, 150, 180, and 200 mm). For some diameters (80 mm) only one L/D value is possible (0.44). For some other diameters, two values of L/D ratios are possible. Both L/D ratio and diameter are considered as discrete inputs.

The hyperbolic tangent is assigned as the activation function to the neurons of the hidden layers while the linear activation function is assigned to the output layer. The random weight initialization of Nguyen and Windrow [26] is adopted for the initialization of weights. Bayesian regularization is also adopted to reduce the effect of weights initialization on network training [27,28].

2.5. Experimental setup

The family of bearings studied in the present work is installed on oil & gas centrifugal compressors. Centrifugal compressors for oil, chemical and gas industry services must comply with American Petroleum Institute (API) standards 617 [29]. The standards define different type of tests with different purposes to ensure equipment reliability and safe installation and operation on site. The mechanical running test (MRT) is one of them and is intended to verify mechanical operation and related monitoring instrumentation such as rotor vibration up to operating and trip speed and bearing metal temperature. The monitoring system is mainly intended for machinery protection and guidelines for its design are given in API 670 [30]. MRT is typically performed with shop driver and shop lube console under vacuum condition to minimize power requirements. This is a mandatory supplier test witnessed by the purchaser before the shipment operation.

During the MRT, rotor speed, bearing oil flow, supply pressure, inlet oil temperature, metal temperatures and rotor vibrations are continuously monitored. In the case of tilting pad journal bearings, the temperature probes are installed on the two most loaded pads at 75% of the pad arc from the leading edge of the pad and at a distance from the white metal sliding surface of 2.5 mm (as prescribed by API 670). The axial position of the probe in the present bearing design was set approximately 20 mm from the outer surface of the pad, see Fig. 1b. In the following section, the MRT bearing data from centrifugal compressors have been compared with the ANN bearing prediction.

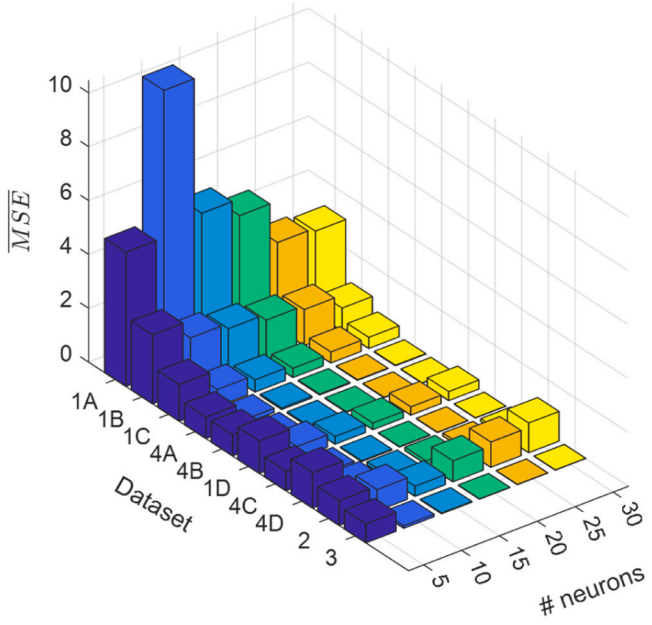

Fig. 4. Average MSE for different combinations of number of neurons and training dataset.

3. Results and discussions

3.1. Training dataset selection

As mentioned in Section 2.3, the dataset investigation is performed only on the 80 mm bearing to reduce the computational time required by the preparation of the training dataset for all diameters belonging to the bearing family. Each dataset (1 A, …, 4D) is used to train neural networks with a different number of neurons. As mentioned in Section 2.4, Bayesian regularization is adopted to reduce the effect of weight initialization. To further limit this, 10 networks are trained for each dataset configuration and number of neurons selected. Each network is then tested on the test dataset. The average Mean square error ($\overline{MSE}$) of the prediction for the 10 networks is taken as an indicator of network accuracy as follow:

$$\overline{MSE} = \frac{1}{n_o}\sum_{n=1}^{n_o}\left(\frac{1}{n_p}\sum_{m=1}^{n_p}(y_m - \widehat{y_m})^2\right) \tag{10}$$

where y_m is the normalized expected output, $\widehat{y_m}$ is the normalized test dataset output, n_p is the number of points in the test dataset, and n_o is the number of the ANN outputs. The $\overline{MSE}$ values calculated for each combination of dataset and number of neurons are shown in Fig. 4. The training datasets are sorted considering the number of points in ascending order.

In general, the accuracy of an ANN increases as the size of the training dataset increases. Moreover, increasing the network size (number of neurons in the hidden layer) should also improve the accuracy. However, for tasks with a relatively low level of complexity, training a complex model increases the risk of overfitting. In general, considering a training dataset, the $\overline{MSE}$ decreases as the number of neurons increases.

The $\overline{MSE}$ values for the training datasets considering an ANN with 10 neurons is shown in Fig. 5a. While the $\overline{MSE}$ values as a function of the number of neurons for datasets 2 and 4B are shown in Fig. 5b.

In Fig. 5a, as expected, the worst accuracy (higher $\overline{MSE}$) is obtained with dataset 1 A and 1B, those characterized by the least number of points. Moreover, the best accuracy is obtained by training the network with dataset 3, the one built with the largest number of points. Interestingly, the accuracy obtained by training the network with datasets 4 A and 4B is much better than that obtained by training the network with datasets 1 C and 1D. As reported in Table 3, datasets 1 C and 1D

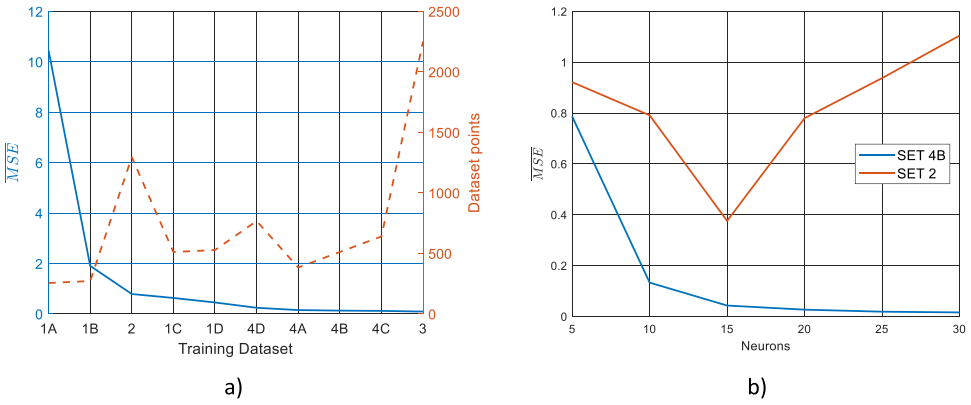

Fig. 5. (a) evolution of $\overline{MSE}$ with the training dataset for the 10-neurons network; (b) evolution of $\overline{MSE}$ with the number of neurons for the 4B and 2 training datasets.

Table 5
Network architectures.

Network	Number of layers	Number of neurons
1	1	10
2	1	20
3	1	30
4	1	40
5	2	10–10
6	2	20–20
7	2	30–30
8	2	40–40

have more points than datasets 4 A and 4B. However, the operational space is better represented by the second pair of datasets, resulting in better network generalization ability. As shown in both Fig. 4 and Fig. 5a, dataset 2 and dataset 4D have similar behavior. Even though they are built with a significant number of data points, the accuracy achieved with networks trained with these two datasets is lower than with training with smaller datasets.

From Fig. 5b it is possible to evaluate the accuracy of the network for a given dataset by increasing the number of neurons. For dataset 4B the accuracy shows a monotonic decreasing trend, where a plateau is reached after 25 neurons. In contrast, for dataset 2 the highest accuracy is obtained with 15 neurons. For larger networks the accuracy is reduced.

From this analysis, dataset 4B was chosen as the best candidate for the training dataset. It ensures a good level of accuracy while keeping the number of training points at a reasonable level. Moreover, the accuracy of the networks trained with dataset 4B shows a monotonic evolution with the number of neurons, as shown in Fig. 5b.

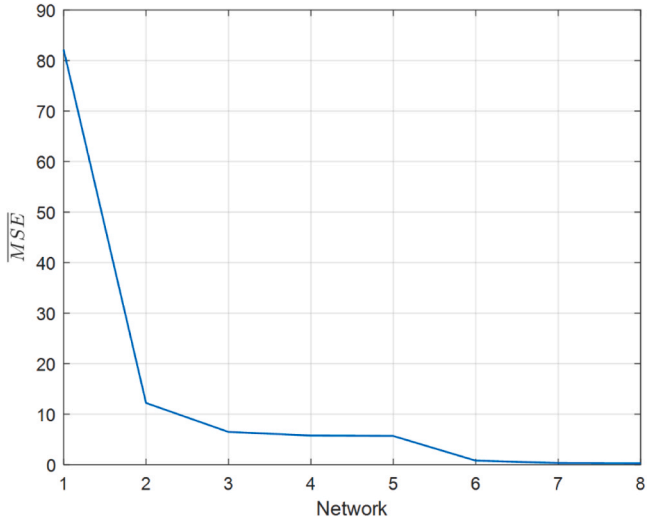

Fig. 6. $\overline{MSE}$ values as a function of the network architectures in Table 5.

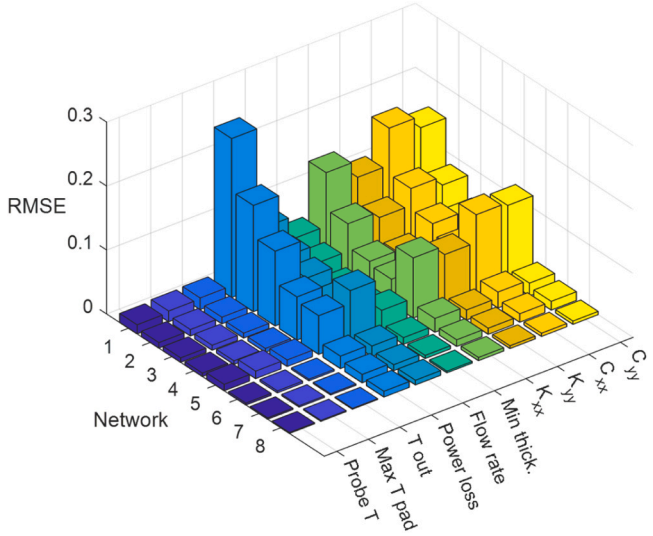

Fig. 7. *RMSE* values for each output and network architecture.

3.2. Network selection for bearing family

Once the training and test datasets were created for all bearing family diameters, an investigation of the network architecture in terms of number of layers and neurons was performed using dataset 4B. For this purpose, a grid-search on the number of hidden layers and hidden neurons is performed. The different architecture tested are listed in Table 5. The network inputs and outputs are listed in Table 4.

The $\overline{MSE}$ value for the different network architectures is shown in Fig. 6. In this case, the accuracy of the network is lower than that showed in Section 3.1. Since all bearing diameters of the bearing family are taken into consideration, the entire training dataset is built with more than 5000 points. At the same time, the size of the networks 1, 2, 3, and 4 is comparable to those considered in Section 3.1. The difficulty level of the task has increased (now all the diameters of the bearing family are considered) while the generalization capacity of the network, related to the number of parameters to be trained, is almost equal to that of Section 3.1. Therefore, the prediction accuracy for single hidden layer networks is lower than that of Section 3.1. When two hidden layers are considered, the generalization ability of the ANN is increases, and the accuracy of the prediction improves.

To better understand the level of accuracy achieved by each network

Table 6
Parameters selected for the 80 mm and 200 mm bearing analysis.

Diameter	80 mm	200 mm
Clearance	Large	Large
L/D ratio	0.44	0.7
Load configuration	LOP	LBP
Oil type	ISO VG 46	ISO VG 46
Inlet pressure	1.1 barG	1.1 barG
Inlet temperatures	50 °C	50 °C
Specific load	0.3–1.5 MPa	0.3–1.5 MPa
Shaft speed	3000 rpm-75 m/s	3000 rpm-75 m/s

for each output, the normalized *RMSE* parameter is considered for each output of the network:

$$RMSE = \sqrt{\frac{1}{n_p}\sum_{m=1}^{n_p}(y_m - \widehat{y_m})^2} \tag{11}$$

The *RMSE* values obtained from each network architecture are shown in Fig. 7. For the sake of clarity, the outputs shown do not include K_{xy}, K_{yx}, C_{xy}, and C_{yx} because the cross dynamic coefficients are quite negligible for TPJBs.

In general, all networks provide good accuracy in predicting oil and probes temperatures. Conversely, the prediction accuracy of the other outputs is strongly affected by the size of the network. The value of the *RMSE* decreases strongly with the increase of the number of neurons and switching to a two-layers network. Considering the results shown in Fig. 7, the network 8 is chosen as the most appropriate one for the analysis.

3.3. ANN estimation of TPJB behavior

The static and dynamic characteristics of the bearings at the extremes of the family, i.e. diameters 80 mm and 200 mm, are studied with the ANN selected in Section 3.2 (dataset 4B and the ANN with two

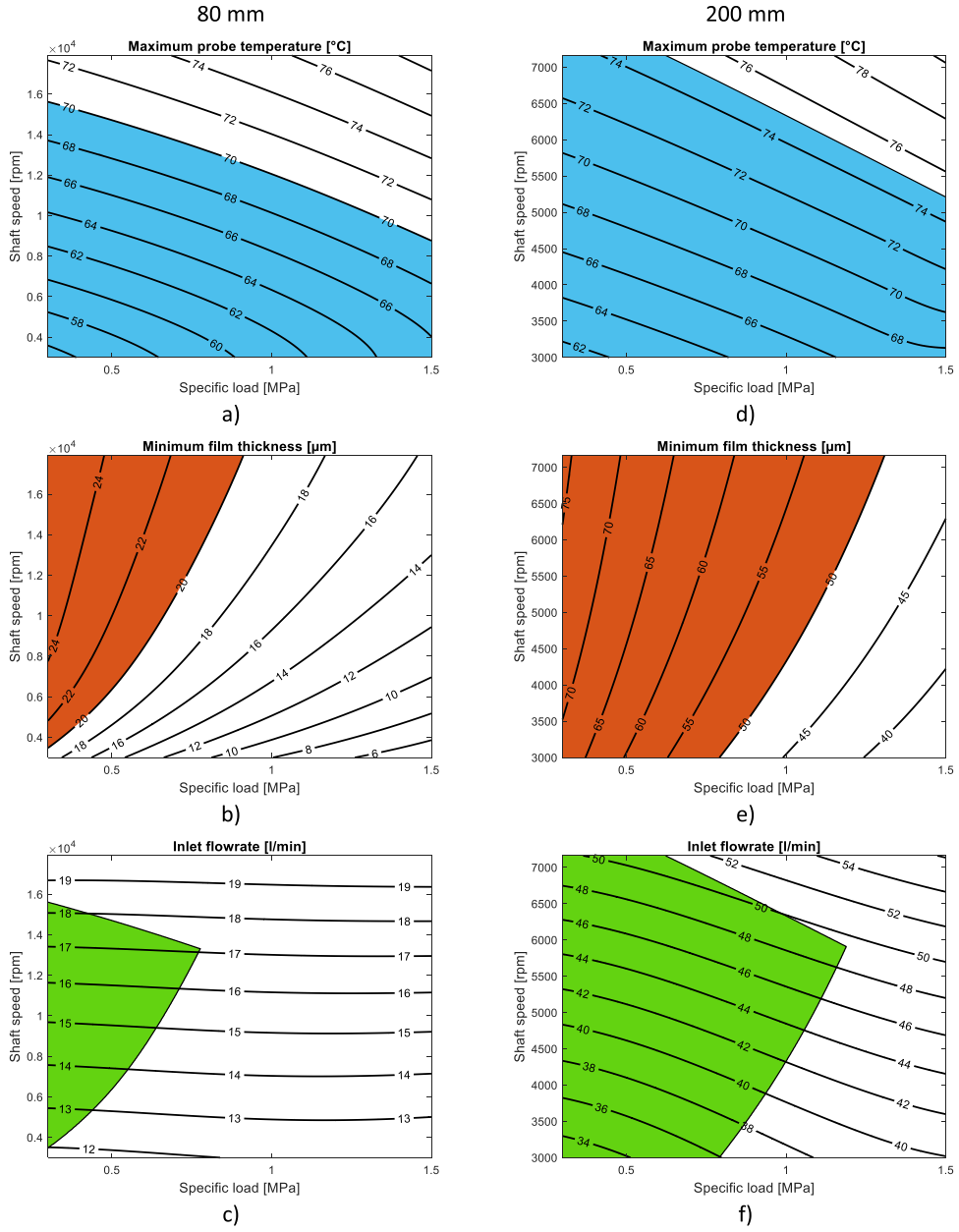

Fig. 8. Evolution of probe temperature a), minimum film thickness b), inlet flowrate c) for 80 mm bearing; evolution of probe temperature d), minimum film thickness e), inlet flowrate f) for 200 mm bearing.

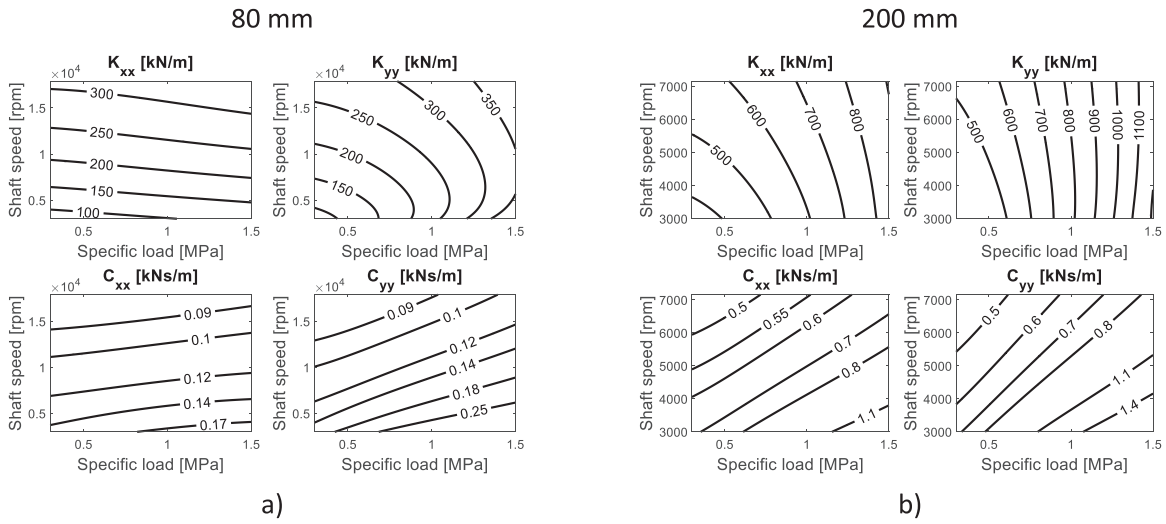

Fig. 9. Evolution of direct stiffness and direct damping coefficients of 80 mm bearing a) and 200 mm bearing b) with shaft speed and load.

hidden layers of 40 neurons each). This analysis allows to demonstrate the ability of the ANN to produce maps describing the evolution of the static characteristics of the bearings with the operating condition. Moreover, similar maps can be obtained for dynamic coefficients which can be used in rotordynamic analysis of turbomachines, especially during the design phase of a new machine where shaft size, load, and speed may change iteratively during the design process.

The parameters selected for the two bearings are listed in Table 6. In this analysis, predictions of bearing behavior provided by the ANN for different specific load and shaft speed are examined. Maps of probe temperature, minimum oil-film thickness and inlet oil flowrate as function of specific load and shaft speed are shown in Fig. 8, whereas dynamic coefficient mapsare shown in Fig. 9.

The results shown refer to the average tolerance values of the bearing microgeometry. As can be seen from Fig. 8, the maximum pad temperature and minimum film thickness are influenced by both shaft speed and specific load. Conversely, the inlet flowrate mainly depends on the shaft speed.

Both the 80 mm and 200 mm configurations have an upper limit for the maximum allowable probe temperature and a lower limit for the minimum allowable oil-film thickness. For the 80 mm bearing the selected limits are respectively $70°C$ for the probe temperature, as indicated in light blue in Figure 8a, and $20\mu m$ for the oil-film thickness, as indicated in light red in Fig. 8b. The safe operating zone that satisfies the two limits for the 80 mm bearing is highlighted by light green in Fig. 8c. Similarly, for the 200 mm bearing the limits are $74°C$ for the probe temperature, and $50\mu m$ for the oil-film. The maps shown in Fig. 8 indicate the ranges of shaft speed and specific load for which the bearing is safely operated, and assist in bearing selection, particularly during the design phase of a new turbomachine.

Maps representing the values of bearing dynamic coefficients as a function of specific load and shaft speed shown in Fig. 9 can help during rotordynamic analysis of turbomachines.

The overall advantage of developing an ANN for static and dynamic characterization of TPJBs is the reduction of computational time required. On a 6-core Intel Core i9–8950HK, the Reynold-based model takes approximately 20 min while the ANN prediction is reached in less than 1 s for each predicted operation point. Creating the training dataset takes a long time. However, once the ANN is trained, the prediction of the dynamic coefficients is almost immediate. Therefore, the developing of the ANN model is convenient if different bearing configurations and operating conditions need to be studied. A great advantage is obtained during the design phase of turbomachines as the geometrical characteristics of the required bearing and the operating conditions can change iteratively. Additionally, the ANN can be implemented within an optimization tool to estimate the minimum flowrate that ensures safe bearing operation while reducing environmental impact.

Table 7
Test configurations of 80 mm and 200 mm bearing for ANN and Reynolds model comparison.

Test configuration	80 mm	200 mm
1	$6000rpm - 0.6MPa$	$3500rpm - 0.6MPa$
2	$6000rpm - 1.4MPa$	$3500rpm - 1.4MPa$
3	$10000rpm - 1.0MPa$	$4500rpm - 1.0MPa$
4	$14000rpm - 0.6MPa$	$5500rpm - 0.6MPa$
5	$14000rpm - 1.4MPa$	$5500rpm - 1.4MPa$

To further emphasize the accuracy of the ANN predictions compared to the Reynolds model predictions, five test configurations of shaft speed and bearing load were selected for both the 80 mm and 200 mm bearing. These test configurations are not present in dataset 4B. The testing configurations are within the operating range defined in Table 6 and are shown in Table 7.

To demonstrate that the chosen test configurations listed in Table 7 are not present in dataset 4B, the combinations of inlet pressure, inlet temperature, specific load, and peripheral speed present in the training dataset for the 80 mm and 200 mm configurations listed in Table 6 are listed in Table 8.

The ANN and Reynolds model predictions of the probe temperature, minimum oil film thickness and inlet flowrate for the 80 mm bearing and 200 mm bearing are shown in Fig. 10.

The ANN and Reynolds model predictions of dynamic stiffness and damping coefficients for the 80 mm bearing and 200 mm bearing are shown in Fig. 11.

As shown in Fig. 10 and Fig. 11, the ANN predictions are practically identical to the prediction of the Reynolds model. Moreover, to further highlight the computational time advantage of the ANN over the Reynolds model, the time required to simulate test configurations with the Reynolds model is comparable to the time required by the ANN to generate the maps shown in Fig. 8 and Fig. 9.

3.4. Comparison with experimental results

In this section, the experimental measurements of probe temperature and inlet flowrate obtained from the MRTs are compared with the numerical predictions obtained with the ANN selected in Section 3.2. For

Table 8
Combinations of inlet temperature, inlet pressure, peripheral speed, and specific load of database 4B for 80 mm and 200 mm bearing in Table 6.

80 mm				200 mm			
Inlet temperature [°C]	Inlet pression [barG]	Peripheral speed [rpm]	Specific load [MPa]	Inlet temperature [°C]	Inlet pressure [barG]	Peripheral speed [rpm]	Specific load [MPa]
40	0.5	17905	0.3	40	0.5	3000	0.3
40	0.5	3000	0.3	40	0.5	7162	0.3
40	0.5	17905	1.5	40	0.5	3000	1.5
40	0.5	3000	1.5	40	0.5	7162	1.5
40	2	17905	0.3	40	2	3000	0.3
40	2	3000	0.3	40	2	7162	0.3
40	2	17905	1.5	40	2	3000	1.5
40	2	3000	1.5	40	2	7162	1.5
40.9	0.97	9521	1.275	40.9	0.97	4821	1.275
42.8	0.78	13247	0.375	42.8	0.78	5861	0.375
44.7	1.53	5795	0.825	44.7	1.53	3780	0.825
46.6	1.34	15110	0.675	46.6	1.34	6382	0.675
48.4	0.59	11384	0.975	48.4	0.59	5341	0.975
50.3	1.91	7658	1.425	50.3	1.91	4301	1.425
52.2	1.16	3932	0.525	52.2	1.16	3260	0.525
54.1	1.72	16973	1.125	54.1	1.72	6902	1.125
55	0.5	17905	0.3	55	0.5	3000	0.3
55	0.5	3000	0.3	55	0.5	7162	0.3
55	0.5	17905	1.5	55	0.5	7162	1.5
55	0.5	3000	1.5	55	2	3000	0.3
55	2	17905	0.3	55	2	7162	0.3
55	2	3000	0.3	55	2	7162	1.5
55	2	17905	1.5	40	0.5	3000	0.3
55	2	3000	1.5	40	0.5	7162	0.3

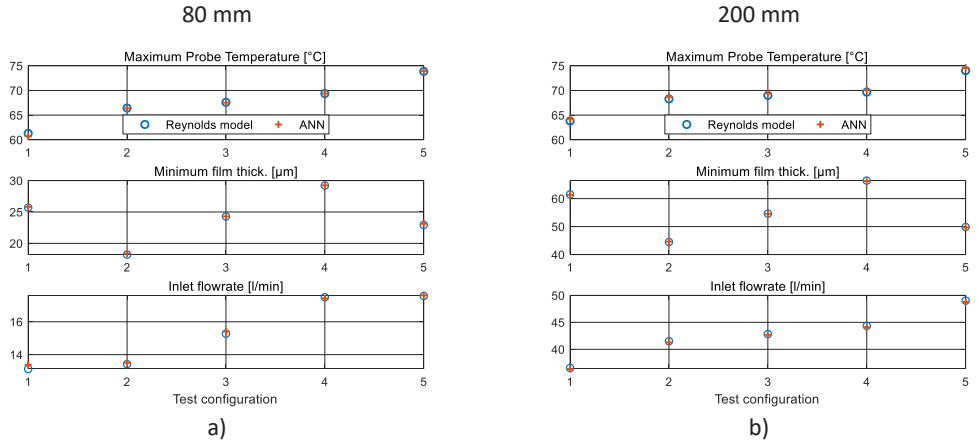

Fig. 10. Comparison of ANN and Reynolds model predictions of maximum probe temperature, minimum film thickness, and inlet flow rate for the test configurations of Table 7 for 80 mm a) and 200 mm b) bearings.

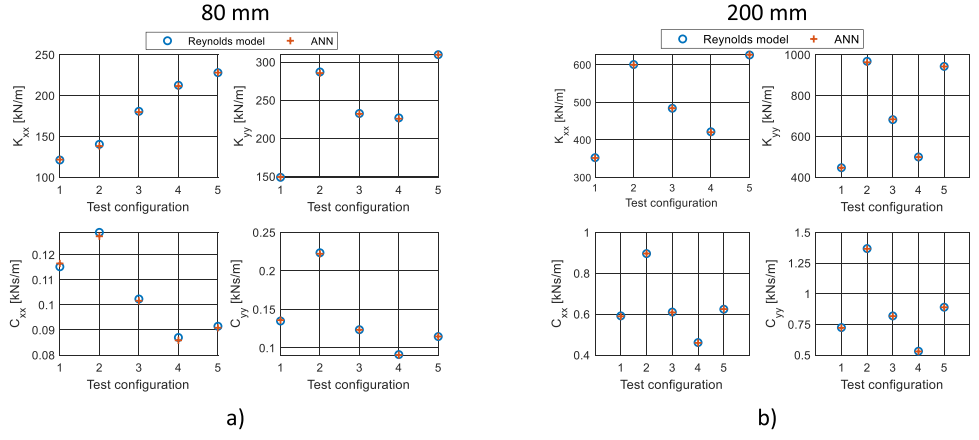

Fig. 11. Comparison of ANN and Reynolds model predictions of dynamic direct stiffness and direct damping coefficients for the test configurations of Table 7 for 80 mm a) and 200 mm b) bearings.

Table 9
Parameters of 80 mm bearing evaluated experimentally.

Parameters	Values
Diameter	80 mm
Clearance	Large
L/D ratio	0.44
Load configuration	LOP
Oil type	ISO VG 32
Inlet pressure	0.3–2 barG
Inlet temperatures	40–55 °C
Specific load	0.23–0.32 MPa
Shaft speed	3000 rpm-75 m/s

Table 10
Parameters of configuration A and configuration B of 200 mm bearing.

	A	B
Diameter	200 mm	200 mm
Clearance	Reduced	Large
L/D ratio	0.7	0.7
Load configuration	LBP	LBP
Oil type	ISO VG 32	ISO VG 32
Inlet pressure	0.3–2 barG	0.3–2 barG
Inlet temperatures	40–55 °C	40–55 °C
Specific load	0.65–0.98 MPa	0.91–1.01 MPa
Shaft speed	3000 rpm-75 m/s	3000 rpm-75 m/s

the 80 mm bearing, a bearing configuration is selected for this analysis, as listed in Table 9. The bearing is tested experimentally at different speeds and for different inlet oil temperatures and pressures, within the allowable range. The different operating points are simply indicated in the following diagrams with cardinal numbers on the x-axis. From the experiments, two values of specific loads are selected: namely 0.23 MPa and 0.32 MPa.

Probe temperature and inlet flowrate predictions for the 80 mm bearing are compared to the experimental values in Fig. 12. Also shown in Fig. 12, a ± 5 °C band of for the numerical probe temperature and a band of ± 10% for the inlet flowrate.

In general, the predictions for the 80 mm bearing are close to the experimental results for both the probe temperature and the inlet flowrate. In Fig. 12 the experimental data comes from two different bearing samples, labeled #1 and #2. The two samples have the same nominal geometry but can differ in machining tolerances.

For the 200 mm bearing, two different configurations are chosen for comparison, labeled as A and B. The two configurations differ in geometry for the type of clearance. The parameters of the two different configurations are listed in Table 10.

Comparisons between the predicted and experimental values of probe temperature and inlet flowrate for the two configurations are shown in Fig. 13 and in Fig. 14, respectively. For configuration A, the experimental data is obtained from two bearing samples with the same nominal geometry. Only one sample is available for configuration B.

For the two configurations the probe temperature measurements are mostly within the ± 5 °C band. Therefore, the temperature prediction can be trusted. With regards to inlet flowrates, for many operating points the measured flowrate is within the ± 10% band of the numerical prediction. The differences in some operating conditions can be ascribed to the experimental setup. For example, the data may have been acquired far from steady-state conditions.

4. Conclusions

In this paper, the development of an ANN to predict the static and dynamic performances of TPJBs is presented. The bearing considered for the analysis differs in term of macro-geometry, micro-geometry, and operating conditions. The main objective of the activity is to obtain a model which, once trained, is able to rapidly and reliably predict both the static and dynamic characteristics of the bearing.

At first, the characteristics of the training database are investigated. Several training datasets in terms of size and operational space coverage are evaluated for the 80 mm bearing. The proposed training datasets are tested with different ANN architectures. The database that ensures an optimal trade-off between prediction accuracy and number of training points is selected as optimal. Once the optimal database architecture was selected, the training databases for all the considered diameters were computed.

The second phase consisted in the analysis of the optimal network architecture for the prediction of the bearing parameters. The network that guarantees the highest accuracy in prediction is made up of two hidden layers of 40 neurons each.

The selected network is then applied to evaluate the static and dynamic performances of the 80 mm and 200 mm bearings. Moreover, the experimental results for the 80 mm and 200 mm bearings are compared with network predictions. For most of the cases, the network's predictions agree well with the experimental results. Therefore, the proposed method is validated and effective in predicting bearing characteristics. The development of the ANN model also guarantees a reduction in the computational time necessary for the calculation of the dynamic coefficients compared to the Reynolds-based model. The ANN model represents an effective and efficient tool to use when it is necessary to estimate the static behavior and the dynamic coefficients of the bearing for different operating conditions and geometric configurations. To increase the generalization and predictability of the ANN it is possible to improve the modeling tool used to build the training dataset.

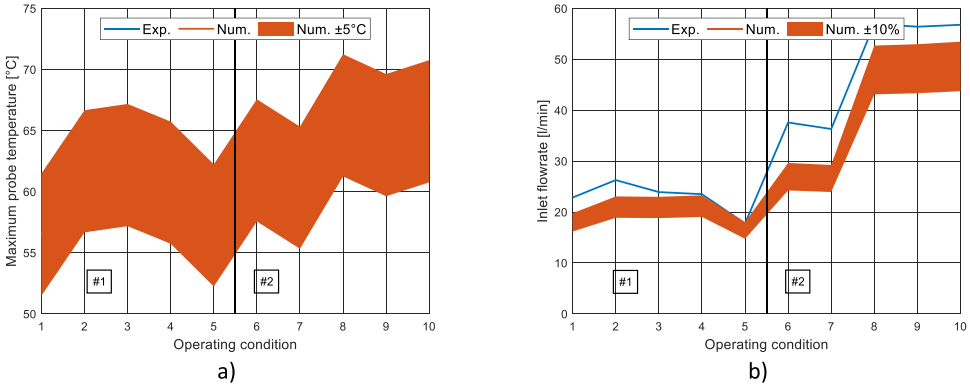

Fig. 12. Comparison of probe maximum temperature a) and oil inlet flowrate b) numerical and experimental results for 80 mm bearing.

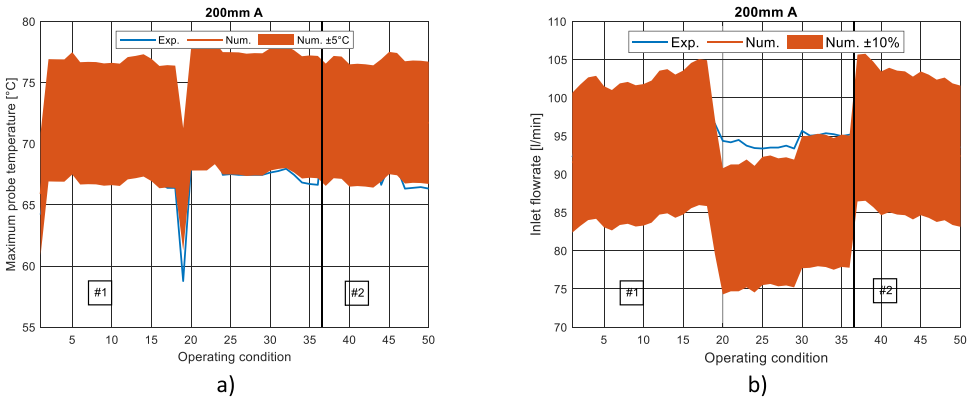

Fig. 13. Comparison of probe maximum temperature a) and oil inlet flowrate b) numerical and experimental results for 200 mm configuration A.

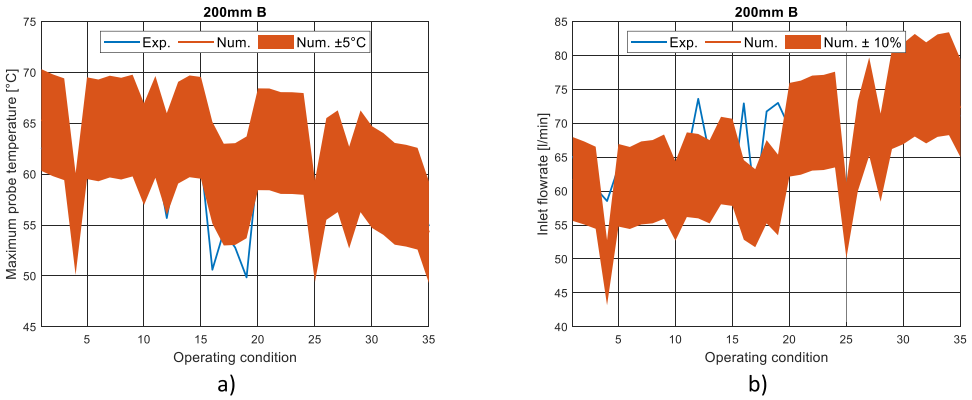

Fig. 14. Comparison of probe maximum temperature a) and oil inlet flowrate b) numerical and experimental results for 200 mm configuration B.

For example, the numerical results obtained from a CFD model can increase the accuracy of predictions regarding inlet flowrate and probe temperature. However, the computational time needed to create the training dataset would increase significantly. Therefore, a trade-off between computational cost and prediction accuracy should be reached.

Declaration of Competing Interest

The authors declare that they have no known competing financial interests or personal relationships that could have appeared to influence the work reported in this paper.

Data Availability

The authors do not have permission to share data.

Acknowledgments

We thank Baker Hughes for funding the project. The rights of all figures are reserved to Baker Hughes Company.

Statement of originality

I confirm that this paper is original and it has not been published previously and it is not under consideration elsewhere.

References

[1] Suh J, Palazzolo A. Three-dimensional dynamic model of TEHD tilting-pad journal bearing—Part I: theoretical modeling. J Tribol 2015:137. https://doi.org/10.1115/1.4030020.

[2] Suh J, Palazzolo A. Three-dimensional dynamic model of TEHD tilting-pad journal bearing—Part II: parametric studies. J Tribol 2015:137. https://doi.org/10.1115/1.4030021.

[3] Yang J, Palazzolo A. Three-dimensional thermo-elasto-hydrodynamic computational fluid dynamics model of a tilting pad journal bearing - Part I: static response. J Tribol 2019:141. https://doi.org/10.1115/1.4043349.

[4] Yang J, Palazzolo A. Three-dimensional thermo-elasto-hydrodynamic computational fluid dynamics model of a tilting pad journal bearing - Part II: dynamic response. J Tribol 2019:141. https://doi.org/10.1115/1.4043350.

[5] Marian M, Tremmel S. Current trends and applications of machine learning in tribology—a review. Lubricants 2021:9. https://doi.org/10.3390/LUBRICANTS9090086.

[6] Rosenkranz A, Marian M, Profito FJ, Aragon N, Shah R. The use of artificial intelligence in tribology—a perspective. Lubricants 2021;9:1–11. https://doi.org/10.3390/lubricants9010002.

[7] Moder J, Bergmann P, Grün F. Lubrication Regime classification of hydrodynamic journal bearings by machine learning using Torque Data. Lubricants 2018:6. https://doi.org/10.3390/lubricants6040108.

[8] Stebakov I, Kornaev A, Popov S, Savin L. Fault diagnosis systems for rotating machines operating with fluid-film bearings. Proc Inst Mech Eng, Part J: J Eng Tribology 2022. https://doi.org/10.1177/13506501211073242.

[9] Katsaros KP, Nikolakopoulos PG. On the tilting-pad thrust bearings hydrodynamic lubrication under combined numerical and machine learning techniques. Lubr Sci 2021;33:153–70. https://doi.org/10.1002/ls.1535.

[10] Katsaros KP, Nikolakopoulos PG. Performance prediction model for hydrodynamically lubricated tilting pad thrust bearings operating under incomplete oil film with the combination of numerical and machine-learning techniques. Lubricants 2023:11. https://doi.org/10.3390/lubricants11030113.

[11] Yang J, Palazzolo A. Computational fluid dynamics based mixing prediction for tilt pad journal bearing TEHD modeling - Part II: Implementation with machine learning. J Tribol 2021:143. https://doi.org/10.1115/1.4047751.

[12] Yang J, Palazzolo A. Tilt pad bearing distributed pad inlet temperature with machine learning-part i: static and dynamic characteristics. J Tribol 2022:144. https://doi.org/10.1115/1.4052171.

[13] Yang J, Palazzolo A. Tilt pad bearing distributed pad inlet temperature with machine learning-Part II: morton effect. J Tribol 2022:144. https://doi.org/10.1115/1.4052172.

[14] Yang J, Palazzolo A. Deep convolutional autoencoder augmented CFD thermal analysis of bearings with inter pad groove mixing. Int J Heat Mass Transf 2022:188. https://doi.org/10.1016/j.ijheatmasstransfer.2022.122639.

[15] Yang J, Palazzolo A. Morton effect prediction with validation using a CFD based CNN for pad inlet temperatures. Mech Syst Signal Process 2023:185. https://doi.org/10.1016/j.ymssp.2022.109827.
[16] Wang N, Tsai C-M. Assessment of artificial neural network for thermohydrodynamic lubrication analysis. Ind Lubr Tribology 2020;72:1233–8. https://doi.org/10.1108/ILT-03-2020-0109.
[17] Roy B, Mukhopadhyay T, Dey S. Polynomial neural network based probabilistic hydrodynamic analysis of two-lobe bearings with stochasticity in surface roughness. Tribol Int 2022:174. https://doi.org/10.1016/j.triboint.2022.107733.
[18] Kazakov YN, Kornaev AV, Shutin DV, Li S, Savin LA. Active fluid-film bearing with deep Q-network agent-based control system. J Tribol 2022:144. https://doi.org/10.1115/1.4053776.
[19] Li S, Zhou C, Savin L, Shutin D, Kornaev A, Polyakov R, et al. Theoretical and experimental study of motion suppression and friction reduction of rotor systems with active hybrid fluid-film bearings. Mech Syst Signal Process 2023:182. https://doi.org/10.1016/j.ymssp.2022.109548.
[20] Dang PV, Chatterton S, Pennacchi P, Vania A. Effect of the load direction on non-nominal five-pad tilting-pad journal bearings. Tribol Int 2016;98:197–211. https://doi.org/10.1016/j.triboint.2016.02.028.
[21] Chatterton S, Pennacchi P, Vania A, Dang PV. Cooled pads for tilting-pad journal bearings. Lubricants 2019:7. https://doi.org/10.3390/lubricants7100092.
[22] Giacopini M, Fowell MT, Dini D, Strozzi A. A mass-conserving complementarity formulation to study lubricant films in the presence of cavitation. J Tribol 2010:132. https://doi.org/10.1115/1.4002215.
[23] Bertocchi L, Dini D, Giacopini M, Fowell MT, Baldini A. Fluid film lubrication in the presence of cavitation: a mass-conserving two-dimensional formulation for compressible, piezoviscous and non-Newtonian fluids. Tribol Int 2013;67:61–71. https://doi.org/10.1016/j.triboint.2013.05.018.
[24] Matlab Deep Learning Toolbox, 1992–2022 The MathWorks, Inc. n.d. https://it.mathworks.com/help/deeplearning/ (Accessed July 27, 2022).
[25] Marquardt D. An algorithm for least-squares estimation of nonlinear parameters. SIAM J Appl Math 1963;11:431–41.
[26] Nguyen D., Widrow B. Improving the learning speed of 2-layer neural networks by choosing initial values of the adaptive weights. 1990 IJCNN International Joint Conference on Neural Networks, 1990, p. 21–6 vol.3. https://doi.org/10.1109/IJCNN.1990.137819.
[27] MacKay DJC. Bayesian Interpolation. Neural Comput 1992;4:415–47. https://doi.org/10.1162/neco.1992.4.3.415.
[28] Dan Foresee F, Hagan MT. Gauss-Newton approximation to bayesian learning. IEEE Int Conf Neural Netw Conf Proc 1997;vol. 3:1930–5. https://doi.org/10.1109/ICNN.1997.614194.
[29] American Petroleum Institute API 617 Standard - Axial and Centrifugal Compressors and Expander-compressors for Petroleum, Chemical and Gas Industry Services, n.d.
[30] American Petroleum Institute API 670 Standard - Machinery Protection System, n.d.